

Electron cooling in graphene thermal transistors

F. Paolucci,^{*,†} F. Bianco,[‡] F. Giazotto,[‡] and S. Roddaro^{*,¶}

[†]*INFN Sezione di Pisa, Largo Bruno Pontecorvo 3, I-56127 Pisa, Italy*

[‡]*NEST, Istituto Nanoscienze-CNR and Scuola Normale Superiore, Piazza San Silvestro 22, I-56127 Pisa, Italy*

[¶]*Dipartimento di Fisica "E. Fermi", Università di Pisa, Largo Bruno Pontecorvo 3, I-56127, Pisa, Italy*

E-mail: federico.paolucci@pi.infn.it; stefano.roddaro@unipi.it

Abstract

In the emergent field of quantum technology, the ability to manage heat at the nanoscale and in cryogenic conditions is crucial for enhancing device performance in terms of noise, coherence, and sensitivity. Here, we demonstrate the active cooling and refrigeration of the electron gas in a graphene thermal transistor, by taking advantage of nanoscale superconductive tunnel contacts able to pump or extract heat directly from the electrons in the device. Our prototypes achieved a top *cooling* of electrons in graphene of ~ 15 mK at a bath temperature of ~ 450 mK, demonstrating the viability of the proposed device architecture. Our experimental findings are backed by a detailed thermal model that accurately replicated the observed device behavior. Alternative cooling schemes and perspectives are discussed in light of the reported results. Finally, our graphene thermal transistor could find application in superconducting hybrid quantum technologies.

Keywords

graphene, superconductors, cooling, electron refrigeration, quantum devices

Introduction

Heat management in nano-scale systems at cryogenic temperatures¹⁻⁴ is the cornerstone for quantum thermodynamics^{5,6} and quantum technology.^{7,8} Indeed, the performance of superconducting quantum devices can be improved by locally decreasing the electronic temperature. In this context, it is possible to distinguish between *cooling*, i.e. leading the electrons colder than the phonons, and *refrigeration*, i.e. actively decreasing the electronic temperature from a maximum to a minimum both larger than the lattice temperature, In particular, local electron cooling in hybrid superconducting systems opens the way to the creation of solid-state heat engines,⁹ by electrical control of the thermal cycles, and to an increase the qubit lifetime,¹⁰ by mastering the quasiparticle population. In addition, direct electron cooling can be a great tool for improving the noise, coherence, and sensitivity of superconducting electronics,^{11,12} magnetometers, or radiation detectors. Indeed, voltage-biased superconducting tunnel junctions are routinely employed to cool electrons in normal metals (NIS coolers)¹³ and superconductors (SIS' coolers).¹⁴ This capability has been exploited to improve the sensitivity of transition-edge sensors (TESs)¹⁵ and to develop the cold-electron bolometers (CEBs).¹⁶ For instance, CEBs showed experimental values of the noise equivalent power (NEP) as low as 3×10^{-18} W Hz^{-1/2},¹⁷ by also leveraging the damping of the electron-phonon thermalization at cryogenic temperatures.¹⁸

In recent years, hybrid superconductor/semiconductor systems gained significant attention in the context of quantum technologies,¹⁹ since they marry the macroscopic phase-coherent nature of superconductors with the field-effect tunability of semiconductors. In particular, proximitized nanowires,²⁰ two-dimensional electron gases (2DEGs)²¹ and graphene^{22,23} have been proposed as the fundamental building blocks of future *gatemon* qubits. Fur-

thermore, superconducting elements coupled to semiconductor quantum dots,²⁴ nanowires²⁵ and graphene^{26,27} have also shown to have promising perspectives as bolometers and single-photon detectors. Among all these hybrid superconductor/semiconductor systems, electron refrigeration was only demonstrated in (i) clean 2DEG/superconductor Josephson junction²⁸ and (ii) InAs nanowire/Al tunnel junctions.²⁹ For what concerns graphene, heat management has only been experimentally achieved in terms of electron-phonon thermalization controlled by overheating the quasiparticles with respect to the lattice, in the limit of ballistic, diffusive and suspended^{30,31} graphene. Despite theoretical studies indicating that graphene-based CEBs achieve very high efficiencies,³² electron cooling has not been demonstrated due to the complexities of the fabrication of high-quality and low-resistance graphene/superconductor tunnel junctions.^{33,34}

Here, we demonstrate graphene electron *refrigeration* and net *cooling* by exploiting superconducting NIS tunnel coolers. To this scope, we designed a thermal transistor, where the graphene channel is in good galvanic contact with metallic source and drain electrodes, thus ensuring efficient heat diffusion in all the device parts. In the studied device, the source electrode is equipped with a tunnel cooler and operates as an electron refrigerator for the whole system; differently, the drain electrode is equipped with local thermometers to monitor the electron temperature throughout the device. This *non-local* geometry allows us to take advantage of the high-quality tunnel barriers achievable in fully metallic junctions,¹⁸ thereby maximizing the device cooling efficiency. As a key technical progress towards the realization of the graphene thermal transistor, we developed a complex fabrication protocol embracing the typical methods of two-dimensional materials and the shadow-mask evaporation technology of fully metallic superconducting devices. In our experiments, we measured electron refrigeration of the drain electrode for a wide range of bath temperatures by voltage-biasing a couple of coolers at the source, demonstrating a best drain cooling of about 3 mK starting from 448 mK. To extract the electronic temperature in the graphene sheet, we developed a theoretical model accounting for all the main thermal exchange mechanisms in the device

and able to fit the experimental data with impressive accuracy. The resulting maximum cooling in graphene was ~ 15 mK at a bath temperature of 448 mK, with a best voltage-to-temperature transfer function of ~ -11.5 mK/ μ V at 307 mK. These results demonstrate that *non-local* electron cooling is a promising strategy for reducing quasiparticle poisoning and noise in hybrid graphene quantum technologies, such as graphene-based coherent electronics, qubits, and radiation detectors.³²

Results and discussion

The studied graphene thermal transistor architecture is shown in Fig. 1a. The realization of the graphene thermal transistor was only possible by introducing the angle controlled shadow-mask evaporation technology in the fabrication protocol of two-dimensional crystal-based devices realized on small chips. In fact, angle resolved evaporation requires homogeneous resist thin films that are usually spin-coated to entire wafers. In our fabrication process, the mechanically exfoliated monolayer graphene flakes were shaped by means of electron-beam lithography (EBL) and reactive ion etching (RIE), while source (S , red), drain (D , orange), coolers (c_i with $i = 1, 2, 3$, yellow) and thermometers (t_i with $i = 1, 2, 3$, yellow) were realized by EBL and shadow mask evaporation through a suspended resist mask. The details of the fabrication procedure are presented in the Methods section.

The rectangular ($8 \times 3 \mu\text{m}^2$) graphene channel (G , grey honeycomb), with electronic temperature T_G , is placed onto an intrinsic silicon substrate covered with a 300 nm-thick silicon dioxide layer (SiO_2 , blue) with phonon temperature T_b . To tune T_G , the graphene is connected through a clean galvanic contact to a non-superconductive S electrode made of $\text{Al}_{0.98}\text{Mn}_{0.02}$, whose temperature (T_S) can be controlled by three tunnel-coupled superconducting aluminum fingers (c_i with $i = 1, 2, 3$, yellow). Indeed, any pair of superconducting tunnel leads can act as a SINIS electron refrigerator for a normal metal island when voltage biased near the sum of their superconducting energy gaps.¹³ Differently, the same electrodes

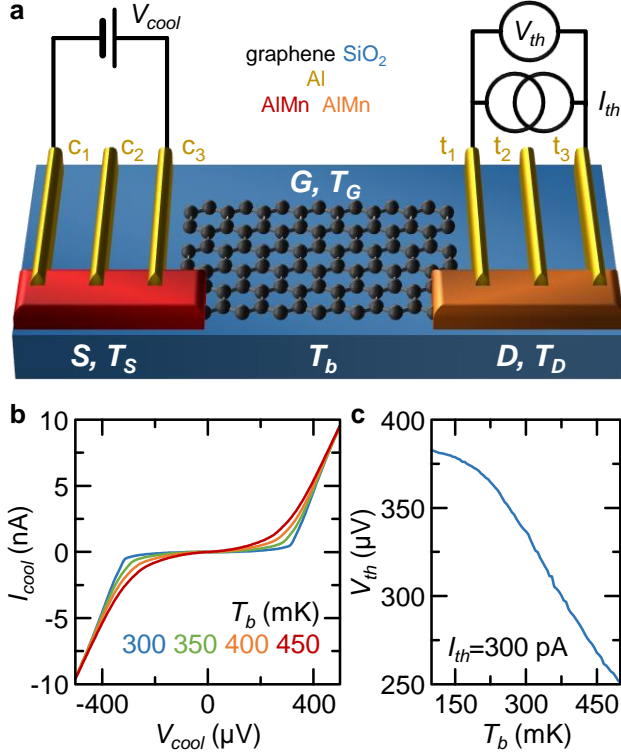


Figure 1: **Schematics and basic characterization of the graphene thermal transistor.** **a** Schematic representation of the device. The electronic temperature (T_S) of the metallic $\text{Al}_{0.98}\text{Mn}_{0.02}$ source electrode (S , red) is decreased/increased with respect to the substrate phonon temperature (T_b) by voltage biasing (V_{cool}) a couple of superconducting Al tunnel coolers (c_1 and c_3 , yellow). The temperature (T_D) of the $\text{Al}_{0.98}\text{Mn}_{0.02}$ drain electrode (D , orange) is measured by current biasing (I_{th}) a couple of superconducting tunnel thermometers (t_1 and t_3 , yellow) while recording the voltage drop (V_{th}). The measured modulation of T_D is due to the change of the graphene electronic temperature (T_G). **b** Current (I_{cool}) versus voltage (V_{cool}) characteristics of the cooling tunnel junctions (c_1 and c_3) for selected values of the bath temperature (T_b). **c** Calibration of the thermometers (t_1 and t_3) in the form of the voltage (V_{th}) versus T_b characteristics at constant current bias $I_{th} = 300$ pA.

act as local heaters when biased in the normal state. Consequently, T_G can be tuned by a voltage (V_{cool}) applied to a pair of cooling junctions thanks to the cold/hot electron diffusion from S to G . To extract the basic properties of all the tunnel coolers, we investigated their transport properties in a two-terminal configuration, as shown in Fig. 1b for c_1 and c_3 at different values of T_b . In particular, we extracted their normal-state resistance ($R_{cool_1} \simeq 3.55$ k Ω , $R_{cool_2} \simeq 22.05$ k Ω and $R_{cool_3} \simeq 17.75$ k Ω) and zero-temperature superconducting energy gap ($\Delta_{0,cool_1} \simeq 175$ μeV , $\Delta_{0,cool_2} \simeq 190$ μeV and $\Delta_{0,cool_3} \simeq 190$ μeV). We note that, according

to the low value of R_{cool_1} , the energy gap of c_1 is lower than that of the other leads since it might be subject to a sizeable inverse proximity effect from S .³⁵ To ensure large cooling power and homogeneity of T_S ,^{13,18} we chose c_1 and c_3 as electronic coolers for our graphene thermal transistor.

The changes of T_G are non-locally detected by measuring the electronic temperature (T_D) of an $\text{Al}_{0.98}\text{Mn}_{0.02}$ metallic drain electrode (D , orange) placed in good electrical contact with G . Indeed, T_D can be probed by current (I_{th}) biasing a couple of superconducting tunnel leads (t_i with $i = 1, 2, 3$, yellow) and recording the voltage drop (V_{th}).³⁶ Since the three electronic thermometers show very similar properties (see Methods for details), we chose to exploit t_1 and t_3 to sample the temperature over the largest possible portion of D . Figure 1c shows the calibration curve of the thermometers (V_{th}) as a function of T_b obtained by injecting $I_{th} = 300$ pA.

The experimental set-up for the investigation of the transport properties of our graphene thermal transistor is sketched in Fig. 1a. The measurements were performed by sweeping V_{cool} while recording T_D . Typically, V_{cool} was swept in the range $-1 \div 1$ mV to probe both cooling (for $|V_{cool}| \lesssim (\Delta_{cool_1} + \Delta_{cool_3})/e$, with e the electron charge) and heating (for $|V_{cool}| > (\Delta_{cool_1} + \Delta_{cool_3})/e$). Furthermore, we determined the impact of phonon temperature by stabilizing the cryostat at desired values of T_b . Figure 2a shows the modulation of T_D with V_{cool} recorded for selected values of T_b . At low values of bath temperature, T_D monotonically increases with $|V_{cool}|$, as shown from the blue trace measured at $T_b = 88$ mK, thus the source serves only as an electron heater. At higher values of T_b , the electronic temperature of D is non-monotonic for a range of V_{cool} that widens with increasing T_b . The graphene thermal transistor shows two distinct operation conditions depending on the bath temperature: in the *cooling* regime T_D is lower than T_b for certain values of V_{cool} (see Fig. 2b), while in the *refrigeration* regime T_D decreases compared to a maximum value ($T_{D,max}$) by increasing V_{cool} but it is always higher than T_b (see Fig. 2c). In particular, the drain electrode shows a maximum cooling of $T_b - T_{D,min} \simeq 3$ mK at $T_b = 448$ mK and the best refrigeration of

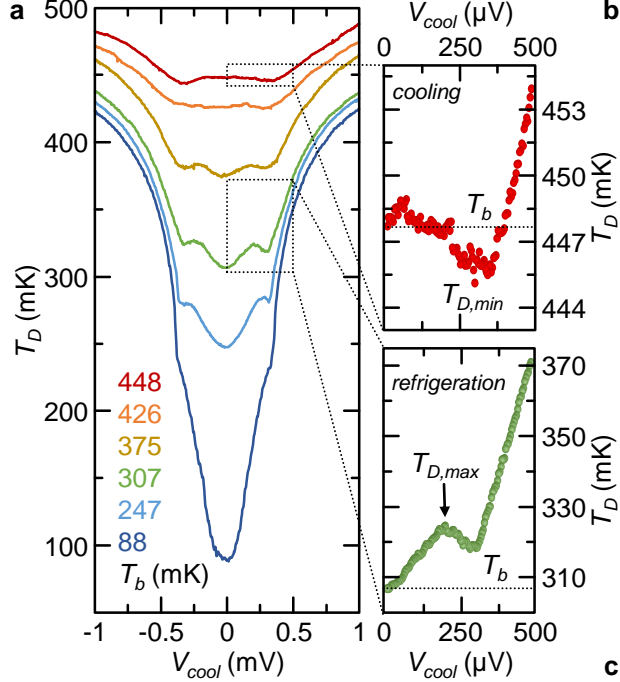


Figure 2: **Temperature modulation of the drain electrode.** **a** Electronic temperature of the drain electrode (T_D) as a function of the voltage bias of the source coolers (V_{cool}) recorded at selected values of bath temperature (T_b). **b** T_D versus V_{cool} characteristics recorded at $T_b = 448$ mK. The system shows *cooling*, that is $T_D < T_b$ for specific values of V_{cool} . $T_{D,min}$ represents the minimum recorded value of T_D . **c** T_D versus V_{cool} characteristics recorded at $T_b = 307$ mK. The system shows *refrigeration*: the coolers are able to decrease the drain temperature from a maximum value ($T_{D,max}$), but $T_D > T_b$ always applies.

$T_{D,max} - T_{D,min} \simeq 5$ mK (with $T_{D,min}$ the minimum temperature recorded) at $T_b = 307$ mK.

The low-voltage electron overheating shown by every experimental curve in Fig. 2a is due to the significant number of under-gap quasiparticle states (described by the Dynes broadening parameter Γ ,³⁷ see Methods) present in the cooler tunnel junctions. In addition, the Joule dissipation (P_J) in S plays a role. These effects fully mask the electron cooling at low bath temperatures, where the electron-phonon thermalization is suppressed and the SINIS coolers are less efficient.^{18,38}

To account for the experimental T_D versus V_{cool} characteristics and to precisely evaluate T_G , we developed a thermal model accounting for all the main exchange mechanisms present in the device, as depicted in Fig. 3a. We assume the phonons in the different elements to

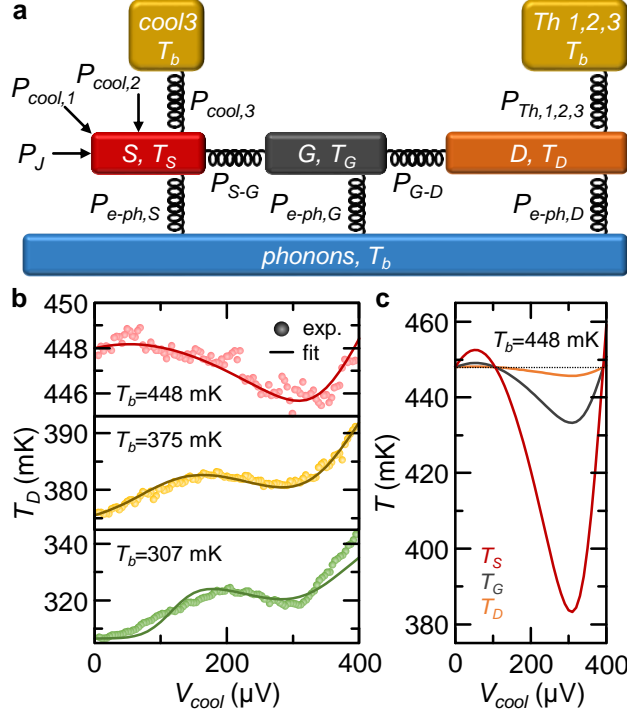


Figure 3: **Thermal modeling of the device, data fitting, and graphene temperature estimation.** **a** Thermal model accounting for the predominant thermal exchange processes in our graphene thermal transistor. The heat interactions between the different elements are indicated by the springs. The sign of the thermal currents depends on the operation regime: refrigeration/cooling or heating. **b** Experimental modulations of T_D (circles) by V_{cool} along with the theoretical model (lines) obtained at $T_b = 448$ mK (red), $T_b = 375$ mK (yellow) and $T_b = 307$ mK (green). **c** Electronic temperature of drain (T_D , orange), graphene (T_G , grey) and source (T_S , red) extracted by fitting the experimental data at $T_b = 448$ mK.

be fully thermalized with the substrate since the Kapitza resistance is negligibly small at sub-kelvin temperatures.³⁹ Furthermore, when power is extracted from (injected to) S by the local coolers, the system operates in the quasi-equilibrium regime:^{18,40} the quasiparticle (electron) populations are described by the Fermi distribution, the electronic temperatures of all the electrodes can be rather different ($T_S \neq T_G \neq T_D$) and out-of-equilibrium with respect to the phonons. Thus, the steady-state temperatures T_S , T_G , and T_D of our thermal

transistor can be calculated through the following system of energy balance equations

$$\left\{ \begin{array}{l} P_{cool_1} + P_{cool_3} + P_J = P_{cool_2} + P_{e-ph,S} + P_{S-G} \\ P_{S-G} = P_{e-ph,G} + P_{G-D} \\ P_{G-D} = P_{e-ph,D} + P_{th_1} + P_{th_2} + P_{th_3}, \end{array} \right. \quad \begin{array}{l} (1.a) \\ (1.b) \\ (1.c) \end{array}$$

where Eq. 1a describes S , Eq. 1b depicts G and Eq. 1c accounts for D . The electrons in S are brought out-of-equilibrium by the power extracted/injected from the biased leads c_1 (P_{cool_1}) and c_3 (P_{cool_3}), and by the I_{cool} -induced Joule dissipation (P_J). These contributions are balanced by the energy exchange with the unbiased tunnel lead (P_{cool_2}), the phonons in S ($P_{e-ph,S}$), and the electrons in the graphene channel (P_{S-G}). The latter is balanced in G by the electron-phonon scattering ($P_{e-ph,G}$) and the electron diffusion towards D (P_{G-D}). Finally, the drain electrons thermalize with the phonons ($P_{e-ph,D}$) and the three thermometers (P_{th_1} , P_{th_2} and P_{th_3}). Concluding, we can exploit Eqs. 1 to fit the experimental data (T_D) and to extract the steady-state values of T_G . The details regarding the theoretical model and each contribution are presented in the Methods section.

Figure 3b shows the comparison between the experimental $T_D(V_{cool})$ characteristics (circles) and the theoretical curves (lines) at selected values of T_b . Despite its apparent complexity, our model provides an excellent agreement with the experimental data both in *cooling* (see the red trace for $T_b = 448$ mK) and *refrigeration* (see the yellow and green curves for $T_b = 375$ mK and $T_b = 307$ mK, respectively). Thus, this model can be exploited to adequately infer the values of T_G and T_D . Indeed, Fig. 3c shows the V_{cool} -dependence of T_S (red), T_G (grey) and T_D (orange) obtained by fitting the experimental data acquired at $T_b = 448$ mK. The temperature modulation strongly reduces from S to D . Indeed, the electrons in S are cooled of ~ 65 mK, in G of ~ 15 mK and in D of ~ 3 mK, thus only about the 4.6% of the energy extracted from (injected in) S is extracted from (injected in) D . By contrast, our device is able to modulate T_G with an efficiency as high as $\sim 23\%$, thereby

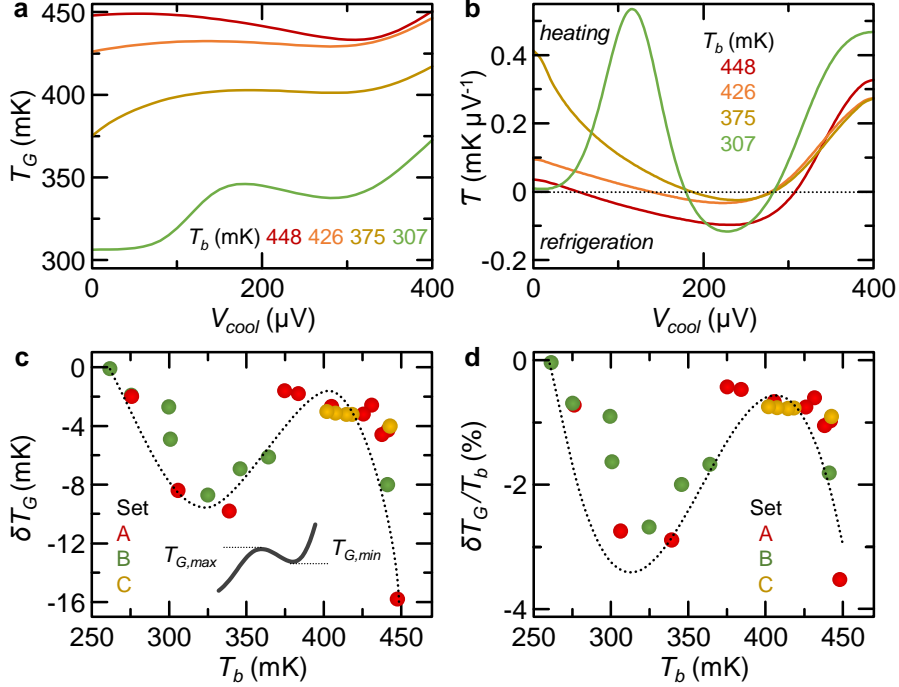


Figure 4: **Electron refrigeration of graphene.** **a** Electronic temperature of graphene (T_G) versus the cooler voltage bias (V_{cool}) extracted for selected values of phonon temperature (T_b). **b** Voltage-to-temperature transfer function ($\mathcal{T} = dT_G/dV_{cool}$) versus cooler voltage bias (V_{cool}) extracted for selected values of phonon temperature (T_b). **c** Electronic refrigeration of graphene ($\delta T_G = T_{G,min} - T_{G,max}$) versus phonon temperature (T_b) extracted for different data sets. The inset schematically depicts the definition of $T_{G,min}$ and $T_{G,max}$. The dotted line is a guide to the eye. **d** Normalized graphene electronic refrigeration ($\delta T_G/T_b$) versus T_b extracted for different data sets. The dotted line is a guide to the eye.

confirming the aptness of the design of our graphene thermal transistor.

We now focus on the refrigeration performance of graphene as a function of voltage bias and bath temperature. Figure 4a shows the V_{cool} -dependence of T_G for selected values of T_b . In full agreement with the measured values of T_D , T_G increases with respect to T_b at low voltage biases, while it decreases when $|V_{cool}| \lesssim (\Delta_{cool_1} + \Delta_{cool_3})/e$. By further raising the voltage bias, the tunnel electrodes act as local heaters and T_G rises monotonically. This phenomenology can be effectively captured by the voltage-to-temperature transfer function, defined as $\mathcal{T} = dT_G/dV_{cool}$, which is a relevant figure of merit for thermal transistors.⁴¹ Indeed, $\mathcal{T} > 0$ indicates that the graphene thermal transistor operates in heating mode, while $\mathcal{T} < 0$ defines refrigeration. The refrigeration efficiency rises with T_b , but the range

of V_{cool} shrinks. In particular, the best cooling efficiency $\mathcal{T} \simeq -11.5 \text{ mK}/\mu\text{V}$ are shown at $V_{cool} = 230 \mu\text{V}$ and $T_b = 307 \text{ mK}$, while the widest range of refrigeration $\delta V_{cool} \simeq 300 \mu\text{K}$ occurs at $T_b = 448 \text{ mK}$.

We now analyse the graphene refrigeration in absolute terms by defining $\delta T_G = T_{G,max} - T_{G,min}$, where $T_{G,max}$ is the maximum value of the graphene temperature for $|V_{cool}| < (\Delta_{cool_1} + \Delta_{cool_3})/e$ and $T_{G,min}$ is the minimum electronic temperature for graphene for $V_{cool} \neq 0$. Figure 4c shows the dependence of δT_G on T_b for three different sets of data (A , B and C). The different data show comparable results, thus confirming both the reproducibility of the thermometry experiments and the accuracy of our model. The raw data and fit of data set B can be found in the SI. Beyond showing larger values of δT_G , the data sets acquired at higher bath temperatures exhibit net *cooling* which reduces from $\sim 15 \text{ mK}$ to $\sim 1 \text{ mK}$ by decreasing T_b . Moreover, the $\delta T_G(T_b)$ characteristics show a strongly non-monotonic oscillatory behavior, since the different thermal conduction channels have completely different temperature dependencies (see the Methods for details). The highest refrigeration was measured at $T_b = 448 \text{ mK}$, since the maximum efficiency of a NIS cooler occurs at $\sim 0.4T_C$ ¹⁸ ($T_b = 448 \text{ mK} \simeq 0.39T_{C,cool_1} \simeq 0.36T_{C,cool_2}$). Finally, we compare δT_G with the initial electronic temperature by defining the normalized graphene electronic refrigeration $\delta T_G/T_b$ shown in Fig. 4d. The maximum normalized refrigeration is about 3.5% at $T_b = 448 \text{ mK}$ and it re-increases to $\sim 3\%$ in the range $300 \text{ mK} \leq T_b \leq 330 \text{ mK}$, pointing out that our graphene thermal transistor can be employed in a wide range of temperatures.

Conclusions

In conclusion, we demonstrated the possibility of refrigerating graphene electrons at cryogenic temperatures. To this scope, we designed and realized a graphene thermal transistor exploiting superconducting tunnel junctions operating as both coolers and thermometers. Thanks to the *non-local* cooling geometry, our device ensures higher cooling efficiency and

lower Joule dissipation compared to direct tunnel refrigeration of graphene electrons in practical settings. In our experiment, the graphene temperature was extracted thanks to a dedicated model accounting for all the main thermal exchange mechanisms present in the system able to precisely fit the measured drain temperature. Interestingly, we demonstrated refrigeration of the graphene electrons by simple voltage in a wide range of bath temperatures (250 – 450 mK). Furthermore, our thermal transistor also showed a net *cooling* of the graphene electrons from the starting phonon temperature with a maximum of ~ 15 mK at $T_b = 448$ mK and a best voltage-to-temperature transfer function of about -11.5 mK/ μ V at $T_b = 307$ mK. The refrigeration efficiency of our graphene thermal transistor could be boosted by decreasing the normal-state resistance of the local tunnel coolers, and by suspending the graphene channel to bring out-of-equilibrium also its phonons.⁴² Furthermore, the drain electrode could be removed to decrease the total thermal losses, since S was only needed to demonstrate the heat diffusion over the whole structure.

Despite directly lowering and measuring the graphene electronic temperature by implementing superconducting tunnel electrodes coupled to G are theoretically possible,³² such a configuration comes with some experimental drawbacks. First, practical superconductor/graphene tunnel junctions exploiting hexagonal boron nitride (hBN) as dielectric material³³ show a lower quality of charge transport compared to fully metallic systems. Second, the tunnel resistivity of hBN is rather large and grows exponentially with the number of layers,³⁴ thus decreasing the cooling efficiency of the superconducting tunnel probe.¹⁸ Third, the charge current necessary to operate tunnel coolers and thermometers would create a sizeable Joule overheating in G , due to the large graphene resistance (normal metal islands have usually resistances of a few ohms), thus compromising the overall cooling efficiency. Consequently, despite the complex structure, our *non-local* configuration promises larger modulations of T_G .

Our thermal transistor could enable the design and realization of innovative devices in the realm of hybrid graphene/superconductor quantum technology. Indeed, the non-local elec-

tron cooling and read-out of graphene cold electron bolometers³² could decrease the noise of the device, since the detector would operate in the graphene idle state (no current flows in the graphene). Furthermore, our graphene electron coolers might be exploited to increase the lifetime of transmon qubits^{22,23} or improve the efficiency of Josephson parametric amplifiers.⁴³ Finally, graphene might be a valid material to increase the tunability and versatility of phase-coherent caloritronics.¹

Methods

Nano-fabrication

The graphene thermal transistor was fabricated onto a $8 \times 8 \text{ m}^2$ chip obtained by dicing a intrinsic silicon wafer covered with 300 nm of thermally grown dry silicon dioxide (SiO_2). To locate the flakes onto the chip, metallic markers were fabricated through electron-beam lithography (EBL) followed by thermal evaporation of 5 nm of Ti and 35 nm of Au. Then, the chip was cleaned by oxygen plasma at 100 W for 5 minutes to remove organic residues on its surface.

Graphene flakes were deposited on the substrate by micro-mechanical exfoliation of natural graphite (NGS Trade and Consulting GmbH) by means of blue tape (Nitto Italia srl). Monolayer flakes were identified by optical contrast and Raman spectroscopy. The $A_G = 8 \times 3 \mu\text{m}^2$ graphene channel of the thermal transistor was shaped by EBL and reactive ion etching (RIE).

The electrodes were fabricated by a single EBL step and two-angle shadow-mask metals deposition through a suspended bilayer resist mask ($\sim 700 \text{ nm}$ -thick MMA film covered by a 250 nm-thick PMMA layer). This technique relies on the strong homogeneity of the resist thin film thickness, thus the spin coating procedure is conventionally performed on an entire wafer. In our fabrication process, the suspended mask was realized on a small substrate by processing graphene flakes in the center of the chip. To have homogeneous films, we employed

a rotation speed of 4000 rpm for both layers. As a result, the central $5 \times 5 \text{ mm}^2$ of the chip are almost homogeneous (a variation $\pm 20 \text{ nm}$), but the MMA film is thinner than usual ($\sim 1.2 \mu\text{m}$), thus allowing for lower shift of the different components of the structure. The evaporation and oxidation processes were performed in an ultra-high vacuum electron-beam evaporator (base pressure of 10^{-11} Torr). At first, 3 nm of Ti and 15 nm of $\text{Al}_{0.98}\text{Mn}_{0.02}$ were deposited at 0° to realize the S and D electrodes (deposition rate $\sim 1.5 \text{ \AA/s}$). The volumes of the Ti and $\text{Al}_{0.98}\text{Mn}_{0.02}$ component of S (D) are $\mathcal{V}_{S,\text{Ti}} \simeq 2.1 \times 10^{-3} \mu\text{m}^3$ ($\mathcal{V}_{D,\text{Ti}} \simeq 1.3 \times 10^{-3} \mu\text{m}^3$) and $\mathcal{V}_{S,\text{AlMn}} \simeq 1.05 \times 10^{-2} \mu\text{m}^3$ ($\mathcal{V}_{D,\text{AlMn}} \simeq 6.6 \times 10^{-3} \mu\text{m}^3$), respectively. Subsequently, the sample was exposed to 200 mTorr of O_2 for 5 min in order to realize the AlO_x thin layer forming the tunnel barriers. Finally, a 35 nm-thick Al layer was deposited at a tilt angle of 40° (deposition rate $\sim 2 \text{ \AA/s}$) to form the superconducting coolers (c_1 , c_2 and c_3) and thermometers (t_1 , t_2 and t_3).

Measurements

All experiments were performed in a filtered $\text{He}^3\text{-He}^4$ dry dilution refrigerator (Triton 200, Oxford Instruments) at bath temperatures ranging from $\sim 90 \text{ mK}$ to $\sim 500 \text{ mK}$.

The charge transport properties of all the tunnel junctions were recorded at different phonon bath temperatures in a standard two-wire configuration by applying a voltage bias through a floating source (GS200, Yokogawa), and by measuring the current with a room-temperature current pre-amplifier (Model 1211, DL Instruments).

The thermal transport experiments were performed by current biasing the SINIS thermometer³⁶ embodied in D by means of a custom-made low-noise floating source ($I_{th} = 300 \text{ pA}$) and monitoring the voltage drop (V_{th}) with a standard room temperature voltage pre-amplifier (Model 1201, DL Instruments). The electronic temperature of S was tuned by voltage biasing a couple of tunnel coolers by a floating source (GS200, Yokogawa). The calibration of the SINIS thermometer was realized by measuring V_{th} at $I_{th} = 300 \text{ pA}$ while slowly varying the cryostat temperature.

Device parameters

Based on the device structure and charge transport experiments, we estimate the basic parameters of our device.

The normal-state resistance of the three cooler tunnel junctions is $R_{cool_1} \simeq 3.55 \text{ k}\Omega$, $R_{cool_2} \simeq 22.05 \text{ k}\Omega$ and $R_{cool_3} \simeq 17.75 \text{ k}\Omega$, respectively. The zero-temperature energy gap of the superconducting coolers is $\Delta_{0,cool_1} \simeq 175 \mu\text{eV}$, $\Delta_{0,cool_2} \simeq 190 \mu\text{eV}$ and $\Delta_{0,cool_3} \simeq 190 \mu\text{eV}$. Consequently, the critical temperature of the three leads is $T_{C,cool_1} \simeq 1.15 \text{ K}$, $T_{C,cool_2} \simeq 1.25 \text{ K}$ and $T_{C,cool_3} \simeq 1.25 \text{ K}$. Finally, the Dynes parameter accounting for sub-gap quasiparticle population³⁷ is $\Gamma_{cool_1} = \Gamma_{cool_2} = \Gamma_{cool_3} = 2 \times 10^{-2}$.

The normal-state resistance of the thermometer tunnel junctions is $R_{th_1} \simeq 26.1 \text{ k}\Omega$, $R_{th_2} \simeq 25 \text{ k}\Omega$ and $R_{th_3} \simeq 26 \text{ k}\Omega$, respectively. The zero-temperatures energy gap of the superconducting thermometers is $\Delta_{0,th_1} \simeq 200 \mu\text{eV}$, $\Delta_{0,th_2} \simeq 200 \mu\text{eV}$ and $\Delta_{0,th_3} \simeq 200 \mu\text{eV}$. The resulting critical temperature of the three probes is $T_{C,th_1} = T_{C,th_2} = T_{C,th_3} \simeq 1.32 \text{ K}$. Finally, the Dynes parameter is $\Gamma_{th_1} = \Gamma_{th_2} = \Gamma_{th_3} = 2 \times 10^{-2}$.

By measuring devices fabricated with the same procedure, we estimated the graphene mobility to be $\mu_G \simeq 10^3 \text{ cm}^2/(\text{V}\cdot\text{s})$. The graphene charge carrier concentration $n_G \simeq 3 \times 10^{12} \text{ cm}^{-2}$ was estimated from the Raman spectra (see Supporting Information). Consequently, the contact resistances of the graphene with the S and D are $R_{S-G} \simeq 15 \text{ k}\Omega$ and $R_{G-D} \simeq 15 \text{ k}\Omega$, respectively.

Theoretical Model

The V_{cool} -dependent experimental values of T_D were fitted for different T_b by exploiting the theoretical model accounting for the main thermal exchange mechanisms present in the device shown in Eq. 1. Here we describe in detail all the contributions.

The energy transfer between a metallic island and a tunnel-coupled superconductor can be

written¹⁸

$$P_k(T_i, T_j) = \frac{1}{e^2 R_k} \int_{-\infty}^{+\infty} d\epsilon \epsilon N_i(\epsilon) [f(\epsilon, T_i) - f(\epsilon + eV, T_j)], \quad (2)$$

where e is the electron charge, R_k is the normal-state resistance of the k tunnel junction, V is the voltage drop across the junction, $N_i(\epsilon)$ is the quasiparticle density of states (DoS) of the superconductor, while $f(\epsilon, T_i)$ and $f(\epsilon + eV, T_j)$ functions of the superconducting i and normal metal j electrode, respectively. The superconducting i -lead shows a smeared BCS DoS $N_i(\epsilon) = |\text{Re}[(\epsilon + i\Delta_{0,i}\Gamma_i)/\sqrt{(\epsilon + i\Delta_{0,i}\Gamma_i)^2 - \Delta_i(T_i)^2}]|$,⁴⁴ where $\Delta_i(T_i)$ is the temperature-dependent energy gap, $\Delta_{0,i}$ the zero-temperature energy gap and Γ_i is the Dynes parameter.³⁷ The power extracted/injected by $cool_1$ ($cool_3$) from/to S P_{cool_1} (P_{cool_3}) can be computed by substituting R_{cool_1} (R_{cool_3}), $\Delta_{0,cool_1}$ ($\Delta_{0,cool_3}$), Γ_{cool_1} (Γ_{cool_3}) and $V = V_{cool}/2$ ($V = V_{cool}/2$) in Eq. 2. Differently, P_{cool_2} is calculated by exploiting $V = 0$, R_{cool_2} , $\Delta_{0,cool_2}$ and Γ_{cool_2} , since $cool_2$ was not biased.

The drain electrode is tunnel coupled to two biased and one unbiased superconducting thermometers. Thus, beyond the constructive parameters of the three junctions, we evaluate P_{th_1} and P_{th_3} at $V = V_{th}/2$, while P_{th_2} is computed at $V = 0$.

The current flowing in S due to the voltage bias applied to the coolers produced a Joule power dissipation

$$P_{Joule}(T_S) = R_S I_{cool}^2(T_S), \quad (3)$$

where $I_{cool}(T_S)$ is the T_S -dependent experimental value of the charge current flowing through the two biased coolers (see Fig. 1b) and R_S is the resistance of the portion of S between the tunnel coolers. The latter is estimated as $R_S = \frac{l_S}{w_S t_S} \frac{1}{e^2 D_{AlMn} N_{AlMn}} = 53.7 \Omega$, with $l_S = 1.5 \mu\text{m}$ the distance between the two coolers, $w_S = 150 \text{ nm}$ the width of the two coolers, $t_S = 15 \text{ nm}$ the film thickness, $D_{AlMn} = 2.25 \times 10^{-3} \text{ m}^2\text{s}^{-1}$ the AlMn diffusion coefficient and $N_{AlMn} = 2.15 \times 10^{47} \text{ m}^{-3}\text{J}^{-1}$ the density of states at the Fermi energy of AlMn. We consider only the conductivity of the AlMn film since the Ti layer acts only as an adhesive layer and does not contribute to the charge transport.

The electron-phonon thermal exchange in the S and D electrodes is described by¹⁸

$$P_{e-ph,i}(T_i, T_b) = \mathcal{V}_{i,Ti} \Sigma_{Ti} (T_i^5 - T_b^5) + \mathcal{V}_{i,AlMn} \Sigma_{AlMn} (T_i^6 - T_b^6), \quad (4)$$

where $\Sigma_{Ti} = 1.3 \times 10^9 \text{ W m}^{-3} \text{ K}^{-5}$ is the electron-phonon coupling constant of Ti, $\Sigma_{AlMn} = 4.5 \times 10^9 \text{ W m}^{-3} \text{ K}^{-6}$ is the electron-phonon scattering constant of $\text{Al}_{0.98}\text{Mn}_{0.02}$ and $i = S, D$. Indeed, the total electron-phonon heat exchange in a metallic thin bilayer is exactly given by the sum of the contributions of the separate components.⁴⁵

The thermal exchange between graphene (G) and the metal electrodes (S and D) can be described by¹⁸

$$P_{i-j}(T_i, T_j) = \frac{\pi^2}{6R_{i-j}} \left(\frac{k_B}{e} \right)^2 (T_i^2 - T_j^2), \quad (5)$$

where $i = S$ and $j = G$ for P_{S-G} , while $i = G$ and $j = D$ for P_{G-D} .

The electron-phonon thermalization in diffusive graphene is given by⁴⁶

$$P_{e-ph,G}(T_G, T_b) = A_G \Sigma_G (T_G^3 - T_b^3). \quad (6)$$

Here, the electron phonon coupling constant can be written $\Sigma_G = \frac{2\zeta(3)D_P^2 k_B^3 e}{\pi^2 \rho_M \hbar^4 v_F^2 v_s^2 \mu_G}$, where $\zeta(3) \simeq 1.2$ is the Apery constant, $D_P = 13 \text{ eV}$ is the deformation potential, $\rho_M = 7.6 \times 10^{-7} \text{ kg/m}^2$ is the mass density, $v_F = 10^6 \text{ m/s}$ is the Fermi velocity and $v_s = 2 \times 10^4 \text{ m/s}$ is the sound velocity of graphene.⁴⁷ Notably, Σ_G is independent of the charge carrier concentration (n_G), thus decreasing the uncertainty on its value.

The validity of our model is confirmed by the accuracy of the fit of the experimental T_D versus V_{cool} characteristics, as shown in Fig. 3b for different values of T_b .

Acknowledgement

The authors thank E. Mangiacotti for fruitful discussions. The work of F. B. and F. P. was partially funded by the Italian Ministry of University and Research under the call

PRIN2022 (Financed by the European Union – Next Generation EU) project EQUATE (Grant No. 2022Z7RHRS). F. G. acknowledges the EU’s Horizon 2020 Research and Innovation Framework Programme under the grants No. 964398 (SUPERGATE), No. 101057977 (SPECTRUM) and the PNRR MUR Project PE000023-NSQTI for partial financial support. S.R. acknowledges the financial support of the TRUST project (PRIN 2022M5RSK5).

Supporting Information Available

The Supporting Information is available free of charge on the ACS Publications website at

Typical Raman spectrum of the graphene channel of our thermal transistor.

Experimental data set B along with the fit obtained by the theoretical model shown in the Methods section.

References

1. Fornieri, A.; Giazotto, F. Towards phase-coherent caloritronics in superconducting circuits. *Nat. Nanotechnol.* **2017**, *12*, 944–952.
2. Roddaro, S.; Pescaglioni, A.; Ercolani, D.; Sorba, L.; Giazotto, F.; Beltram, F. Hot-electron effects in InAs nanowire Josephson junctions. *Nano Res.* **2011**, *4*, 259–265.
3. Fornieri, A.; Martínez-Pérez, M. J.; Giazotto, F. A normal metal tunnel-junction heat diode. *Appl. Phys. Lett.* **2014**, *104*, 183108.
4. Guarcello, C.; Solinas, P.; Braggio, A.; Di Ventra, M.; Giazotto, F. Josephson Thermal Memory. *Phys. Rev. Appl.* **2018**, *9*.
5. Lieb, E. H.; Yngvason, J. The physics and mathematics of the second law of thermodynamics. *Physics Reports* **1999**, *310*, 1–96.

6. Horodecki, M.; Oppenheim, J. Fundamental limitations for quantum and nanoscale thermodynamics. *Nat. Commun.* **2013**, *4*, 2059.
7. Gao, Y. Y.; Rol, M. A.; Touzard, S.; Wang, C. Practical Guide for Building Superconducting Quantum Devices. *PRX Quantum* **2021**, *2*, 040202.
8. Acín, A.; Bloch, I.; Buhrman, H.; Calarco, T.; Eichler, C.; Eisert, J.; Esteve, D.; Gisin, N.; Glaser, S. J.; Jelezko, F.; Kuhr, S.; Lewenstein, M.; Riedel, M. F.; Schmidt, P. O.; Thew, R.; Wallraff, A.; Walmsley, I.; Wilhelm, F. K. The quantum technologies roadmap: a European community view. *New J. Phys.* **2018**, *20*, 080201.
9. Germanese, G.; Paolucci, F.; Marchegiani, G.; Braggio, A.; Giazotto, F. Bipolar thermoelectric Josephson engine. *Nat. Nanotechnol.* **2022**, *17*, 1084–1090.
10. Verjauw, J.; Acharya, R.; Van Damme, J.; Ivanov, T.; Lozano, D. P.; Mohiyaddin, F. A.; Wan, D.; Jussot, J.; Vadiraj, A. M.; Mongillo, M.; Heyns, M.; Radu, I.; Govoreanu, B.; Potočník, A. Path toward manufacturable superconducting qubits with relaxation times exceeding 0.1 ms. *Npj Quantum Inf.* **2022**, *8*.
11. Giazotto, F.; Pekola, J. P. Josephson tunnel junction controlled by quasiparticle injection. *J. Appl. Phys.* **2005**, *97*, 023908.
12. Tirelli, S.; Savin, A. M.; Garcia, C. P.; Pekola, J. P.; Beltram, F.; Giazotto, F. Manipulation and generation of supercurrent in out-of-equilibrium Josephson tunnel nanojunctions. *Phys. Rev. Lett.* **2008**, *101*, 077004.
13. Nahum, M.; Eiles, T. M.; Martinis, J. M. Electronic microrefrigerator based on a normal-insulator-superconductor tunnel junction. *Applied Physics Letters* **1994**, *65*, 3123–3125.
14. Quaranta, O.; Spathis, P.; Beltram, F.; Giazotto, F. Cooling electrons from 1 to 0.4 K with V-based nanorefrigerators. *Applied Physics Letters* **2011**, *98*, 032501.

15. Miller, N. A.; O’Neil, G. C.; Beall, J. A.; Hilton, G. C.; Irwin, K. D.; Schmidt, D. R.; Vale, L. R.; Ullom, J. N. High resolution x-ray transition-edge sensor cooled by tunnel junction refrigerators. *Applied Physics Letters* **2008**, *92*, 163501.
16. Kuzmin, L. S. On the concept of a hot-electron microbolometer with capacitive coupling to the antenna. *Physica B: Condensed Matter* **2000**, *284-288*, 2129–2130.
17. Kuzmin, L. S.; Pankratov, A. L.; Gordeeva, A. V.; Zbrozhek, V. O.; Shamporov, V. A.; Revin, L. S.; Blagodatkin, A. V.; Masi, S.; de Bernardis, P. Photon-noise-limited cold-electron bolometer based on strong electron self-cooling for high-performance cosmology missions. *Commun. Phys.* **2019**, *2*.
18. Giazotto, F.; Heikkilä, T. T.; Luukanen, A.; Savin, A. M.; Pekola, J. P. Opportunities for mesoscopics in thermometry and refrigeration: Physics and applications. *Rev. Mod. Phys.* **2006**, *78*, 217–274.
19. Benito, M.; Burkard, G. Hybrid superconductor-semiconductor systems for quantum technology. *Applied Physics Letters* **2020**, *116*, 190502.
20. Casparis, L.; Larsen, T. W.; Olsen, M. S.; Kuemmeth, F.; Krogstrup, P.; Nygård, J.; Petersson, K. D.; Marcus, C. M. Gatemon Benchmarking and Two-Qubit Operations. *Phys. Rev. Lett.* **2016**, *116*, 150505.
21. Casparis, L.; Connolly, M. R.; Kjaergaard, M.; Pearson, N. J.; Kringhøj, A.; Larsen, T. W.; Kuemmeth, F.; Wang, T.; Thomas, C.; Gronin, S.; Gardner, G. C.; Manfra, M. J.; Marcus, C. M.; Petersson, K. D. Superconducting gatemon qubit based on a proximitized two-dimensional electron gas. *Nat. Nanotechnol.* **2018**, *13*, 915–919.
22. Kroll, J. G.; Uilhoorn, W.; van der Enden, K. L.; de Jong, D.; Watanabe, K.; Taniguchi, T.; Goswami, S.; Cassidy, M. C.; Kouwenhoven, L. P. Magnetic field compatible circuit quantum electrodynamics with graphene Josephson junctions. *Nat. Commun.* **2018**, *9*, 4615.

23. Wang, J. I.-J.; Rodan-Legrain, D.; Bretheau, L.; Campbell, D. L.; Kannan, B.; Kim, D.; Kjaergaard, M.; Krantz, P.; Samach, G. O.; Yan, F.; Yoder, J. L.; Watanabe, K.; Taniguchi, T.; Orlando, T. P.; Gustavsson, S.; Jarillo-Herrero, P.; Oliver, W. D. Coherent control of a hybrid superconducting circuit made with graphene-based van der Waals heterostructures. *Nat. Nanotechnol.* **2019**, *14*, 120–125.
24. Komiyama, S.; Astafiev, O.; Antonov, V., V; Kutsuwa, T.; Hirai, H. A single-photon detector in the far-infrared range. *Nature* **2000**, *403*, 405–407.
25. Schäpers, T.; Müller, R. P.; Kaluza, A.; Hardtdegen, H.; Lüth, H. Adjustment of the critical current in a Nb-In x Ga $1-x$ As/InP Josephson contact by light exposure. *Applied Physics Letters* **1999**, *75*, 391–393.
26. Lee, G.-H.; Efetov, D. K.; Jung, W.; Ranzani, L.; Walsh, E. D.; Ohki, T. A.; Taniguchi, T.; Watanabe, K.; Kim, P.; Englund, D.; Fong, K. C. Graphene-based Josephson junction microwave bolometer. *Nature* **2020**, *586*, 42–46.
27. Walsh, E. D.; Jung, W.; Lee, G.-H.; Efetov, D. K.; Wu, B.-I.; Huang, K.-F.; Ohki, T. A.; Taniguchi, T.; Watanabe, K.; Kim, P.; Englund, D.; Fong, K. C. Josephson junction infrared single-photon detector. *Science* **2021**, *372*, 409–412.
28. Gunnarsson, D.; Richardson-Bullock, J. S.; Prest, M. J.; Nguyen, H. Q.; Timofeev, A. V.; Shah, V. A.; Whall, T. E.; Parker, E. H. C.; Leadley, D. R.; Myronov, M.; Prunnila, M. Interfacial engineering of semiconductor-superconductor junctions for high performance micro-coolers. *Sci. Rep.* **2015**, *5*, 17398.
29. Mastomäki, J.; Roddaro, S.; Rocci, M.; Zannier, V.; Ercolani, D.; Sorba, L.; Maasilta, I. J.; Ligato, N.; Fornieri, A.; Strambini, E.; Giazotto, F. InAs nanowire superconducting tunnel junctions: Quasiparticle spectroscopy, thermometry, and nanorefrigeration. *Nano Res.* **2017**, *10*, 3468–3475.

30. Betz, A. C.; Jhang, S. H.; Pallecchi, E.; Ferreira, R.; Fève, G.; Berroir, J.-M.; Plaçais, B. Supercollision cooling in undoped graphene. *Nat. Phys.* **2013**, *9*, 109–112.
31. Laitinen, A.; Oksanen, M.; Fay, A.; Cox, D.; Tomi, M.; Virtanen, P.; Hakonen, P. J. Electron-phonon coupling in suspended graphene: supercollisions by ripples. *Nano Lett.* **2014**, *14*, 3009–3013.
32. Vischi, F.; Carrega, M.; Braggio, A.; Paolucci, F.; Bianco, F.; Roddaro, S.; Giazotto, F. Electron Cooling with Graphene-Insulator-Superconductor Tunnel Junctions for Applications in Fast Bolometry. *Phys. Rev. Appl.* **2020**, *13*, 054006.
33. Bretheau, L.; Wang, J. I.-J.; Pisoni, R.; Watanabe, K.; Taniguchi, T.; Jarillo-Herrero, P. Tunnelling spectroscopy of Andreev states in graphene. *Nature Physics* **2017**, *13*, 756–760.
34. Lee, G.-H.; Yu, Y.-J.; Lee, C.; Dean, C.; Shepard, K. L.; Kim, P.; Hone, J. Electron tunneling through atomically flat and ultrathin hexagonal boron nitride. *Applied Physics Letters* **2011**, *99*, 243114.
35. De Gennes, P. G. *Superconductivity of Metals and Alloys*; Advanced book classics; Perseus: Cambridge, MA, 1999.
36. Rowell, J. M.; Tsui, D. C. Hot electron temperature in InAs measured by tunneling. *Phys. Rev. B* **1976**, *14*, 2456–2463.
37. Dynes, R. C.; Garno, J. P.; Hertel, G. B.; Orlando, T. P. Tunneling Study of Superconductivity near the Metal-Insulator Transition. *Phys. Rev. Lett.* **1984**, *53*, 2437–2440.
38. Pekola, J. P.; Heikkilä, T. T.; Savin, A. M.; Flyktman, J. T.; Giazotto, F.; Hekking, F. W. J. Limitations in Cooling Electrons using Normal-Metal-Superconductor Tunnel Junctions. *Phys. Rev. Lett.* **2004**, *92*, 056804.

39. Wellstood, F. C.; Urbina, C.; Clarke, J. Hot-electron effects in metals. *Phys. Rev. B* **1994**, *49*, 5942–5955.
40. Muhonen, J. T.; Meschke, M.; Pekola, J. P. Micrometre-scale refrigerators. *Reports on Progress in Physics* **2012**, *75*, 046501.
41. Paolucci, F.; Marchegiani, G.; Strambini, E.; Giazotto, F. Phase-tunable temperature amplifier. *Europhysics Letters* **2017**, *118*, 68004.
42. Koppinen, P. J.; Maasilta, I. J. Phonon Cooling of Nanomechanical Beams with Tunnel Junctions. *Phys. Rev. Lett.* **2009**, *102*, 165502.
43. Butseraen, G.; Ranadive, A.; Aparicio, N.; Rafsanjani Amin, K.; Juyal, A.; Esposito, M.; Watanabe, K.; Taniguchi, T.; Roch, N.; Lefloch, F.; Renard, J. A gate-tunable graphene Josephson parametric amplifier. *Nat. Nanotechnol.* **2022**, *17*, 1153–1158.
44. Tinkham, M. *Introduction to Superconductivity*, 2nd ed.; Dover Publications, 2004.
45. Paolucci, F.; Buccheri, V.; Germanese, G.; Ligato, N.; Paoletti, R.; Signorelli, G.; Bitossi, M.; Spagnolo, P.; Falferi, P.; Rajteri, M.; Gatti, C.; Giazotto, F. Development of highly sensitive nanoscale transition edge sensors for gigahertz astronomy and dark matter search. *Journal of Applied Physics* **2020**, *128*, 194502.
46. Chen, W.; Clerk, A. A. Electron-phonon mediated heat flow in disordered graphene. *Phys. Rev. B* **2012**, *86*, 125443.
47. Castro Neto, A. H.; Guinea, F.; Peres, N. M. R.; Novoselov, K. S.; Geim, A. K. The electronic properties of graphene. *Rev. Mod. Phys.* **2009**, *81*, 109–162.

Supporting Information: Electron cooling in graphene thermal transistors

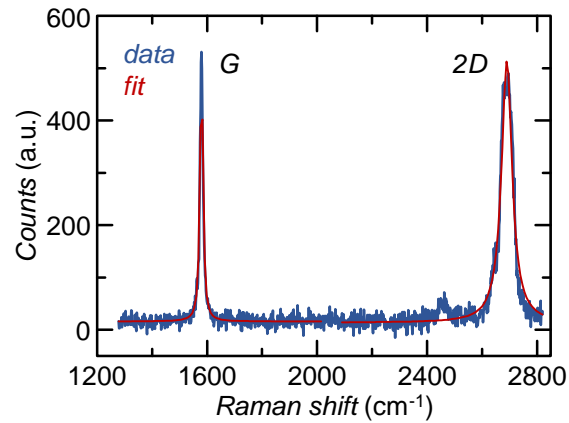


Figure 5: **Raman spectroscopy.** Typical Raman spectrum of the graphene channel of our thermal transistor (blue) along with the Lorentzian fit (red) of the G and $2D$ peaks. The position of the two Raman modes is $\sim 1582.7 \text{ cm}^{-1}$ and $\sim 2676.5 \text{ cm}^{-1}$ for the G and $2D$ peak, respectively. By constructing the related correlation plot,¹ we extracted a small strain ($\sim 0.1\%$) and a charge concentration $n_G \simeq 3 \times 10^{12} \text{ cm}^{-2}$ for the graphene channel.

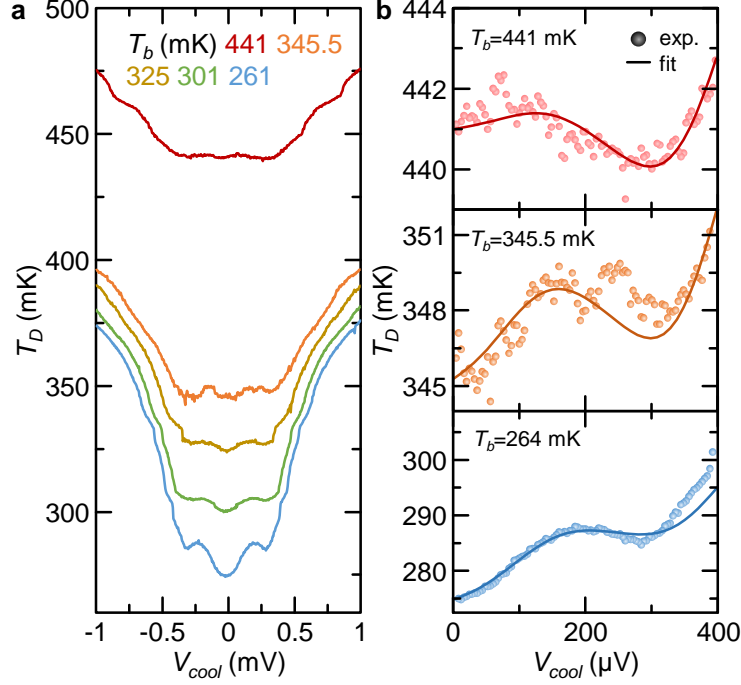


Figure 6: **Temperature modulation of the drain electrode for data set B.** **a** Electronic temperature of the drain electrode (T_D) as a function of the voltage bias of the source coolers (V_{cool}) recorded at selected values of phonon temperature (T_b). **b** Experimental modulations of T_D (circles) by V_{cool} along with the theoretical model (lines) obtained at $T_b = 441$ mK (red), $T_b = 345.5$ mK (orange) and $T_b = 264$ mK (turquoise).

References

1. Lee, J. E.; Ahn, G.; Shim, J.; Lee, Y. S.; Ryu, S. Optical separation of mechanical strain from charge doping in graphene. *Nat. Commun.* **2012**, *3*, 1024.

TOC Graphic

